Geochemistry Geophysics Geosystems G3

Article
Volume 14, Number 1
31 January 2013
doi:10.1029/2012GC004383
ISSN: 1525-2027

Published by AGU and the Geochemical Society

Dynamics of a laminar plume in a cavity: The influence of boundaries on the steady state stem structure

P. E. van Keken
Department of Earth and Environmental Sciences, University of Michigan, Ann Arbor, Michigan, USA (keken@umich.edu)

A. Davaille
Laboratoire FAST, Université Paris-Sud, Orsay, France

J. Vatteville
LDFG, Institut de Physique du Globe de Paris, Paris, France

Laboratoire FAST, Université Paris-Sud, Orsay, France

[1] The steady state structure of thermal plumes rising from a small heater is studied in high Prandtl number fluids. We show good agreement between laboratory experiments and numerical simulations. We study the effect of the boundaries on the plume development by numerically simulating the plume rise in very large geometries. The thermal structure of the plume axis is similar for all box sizes considered, but the velocity structure changes strongly as box sizes are increased. We show that the effect of the side boundaries becomes unimportant for large aspect ratio, but that the free-slip top boundary has a strong influence on the velocity structure under all conditions. We show that the use of an outflow boundary condition significantly reduces the influence of the top boundary. Under these conditions we recover to good precision the theoretical predictions for plumes rising in an semi-infinite half-space. The strong influence of the boundaries in high Prandtl number fluids is important in the interpretation of laboratory experiments and numerical simulation for the dynamics of the Earth's mantle.

Components: 9,800 words, 15 figures.

Keywords: laboratory experiments; geodynamics; mantle plumes; hot spots.

Index Terms: 0550 Computational Geophysics: Model verification and validation; 8137 Tectonophysics: Hotspots, large igneous provinces, and flood basalt volcanism; 8121 Tectonophysics: Dynamics: convection currents, and mantle plumes.

Received 9 August 2012; **Revised** 15 November 2012; **Accepted** 15 November 2012; **Published** 31 January 2013.

van Keken, P. E., A. Davaille, and J. Vatteville (2013), Dynamics of a laminar plume in a cavity: The influence of boundaries on the steady state stem structure, *Geochem. Geophys. Geosyst.*, *14*, 158–178, doi:10.1029/2012GC004383.

1. Introduction

1.1. Mantle Convection and Plumes

[2] Slow convection in the Earth's mantle is expressed at the surface by creation of plates at midoceanic ridges and subsequent destruction of the plates upon subduction at convergent margins with related volcanism. Hot spots such as Hawai'i and Iceland are characterized by midplate volcanism or excess volcanism at ridges. These hot spot regions appear to be supported by the long-term presence of hot material below the lithosphere. The best fluid dynamical explanation for hotspots remains the rise of mantle plumes, which are columnar upwellings with vertical speeds that are significantly higher than they move laterally [e.g., *Morgan*, 1971]. These plumes are ubiquitous features of thermal convection in viscous fluids. Fluid dynamical modeling using laboratory experiments, theoretical arguments, and numerical simulations (for recent reviews, see *Ribe et al*. [2006], *Ito and van Keken* [2007], and *Davaille and Limare* [2007]) demonstrates that the physical characteristics of hotspots in many cases can be explained by plumes rising from the deep mantle, although shallow mantle origins have also been suggested [*King and Ritsema*, 2000]. Seismological evidence for low velocity regions below hotspots have also been used to argue for the existence of plumes [*Montelli et al*., 2004; *Wolfe et al*., 2009], although it is likely that application of standard tomographic techniques is limited due to the effects of wave front healing that may render plumes invisible in the deeper mantle [*Hwang et al*., 2011].

[3] In order to improve our understanding of the formation of hotspots in the convecting mantle, it is essential to develop a strong fluid dynamical basis for studying the development of mantle plumes. Numerous studies have been devoted to that task in the last 50 years. The temperature is hot and uniform over the whole core-mantle boundary and several plumes are expected to develop from the hot thermal boundary layer there. However, in order to better focus on the development of a single plume, a small patch heated at constant temperature can be taken as a proxy. This confined heat source ensures that only one plume is generated, and that it evolves to a quasi steady state. This is the geometry that we shall also adopt in this study.

[4] *Turner* [1962] was the first to study what he called the starting plume, comprising a steady plume conduit capped by a large buoyant head. He further suggested that the buoyancy of the head increases since the head is fed by the stem as a result of the slower upwards motion of the head compared with the steady stem below it. Since then, much effort has been devoted to understand plume dynamics and to provide scalings for plume ascent velocity [*Whitehead and Luther*, 1975; *Shlien*, 1976; *Olson and Singer*, 1985; *Chay and Shlien*, 1986; *Griffiths and Campbell*, 1990; *Moses et al*., 1993; *Couliette and Loper*, 1995; *van Keken*, 1997; *Kaminski and Jaupart*, 2003; *Rogers and Morris*, 2009; *Davaille et al*., 2011] or for steady state plume stem structure [*Batchelor*, 1954; *Fujii*, 1962; *Shlien and Boxman*, 1979; *Tanny and Shlien*, 1985; *Worster*, 1986; *Moses et al*., 1993; *Olson et al*., 1993; *Couliette and Loper*, 1995; *Vasquez et al*., 1996; *Laudenbach and Christensen*, 2001; *Whittaker and Lister*, 2006a, 2006b; *Davaille et al*., 2011]. Additionally, plume growth by entrainment of fluid by thermal diffusion, continuous feeding from the source, laminar entrainment of surrounding material at the rear of a leading vortical head has been studied [*Griffiths and Campbell*, 1990; *Moses et al*., 1993; *Couliette and Loper*, 1995; *Kumagai*, 2002]. It is well recognized that plume morphology and time evolution can be complex due to phase changes, rheological variations, mean ambient shear flow, and compositional effects [e.g., *Bercovici and Mahoney*, 1994; *van Keken*, 1997; *Thompson and Tackley*, 1998; *Davaille*, 1999; *Farnetani and Samuel*, 2005; *Lin and van Keken*, 2005; *Kumagai et al*., 2008].

[5] Although the different studies generally agree on the broad picture of plume dynamics, they often propose quantitatively different scalings. One reason probably resides in the differences in boundary conditions adopted by the authors. Theoretical studies often need to assume an infinite or semi-infinite fluid, while laboratory experiments generally use rigid bottom and side boundaries and deformable or rigid top boundary. On the other hand, numerical studies for a long time preferentially prescribed free-slip nondeformable boundaries. In some cases, rigid boundaries [e.g., *Blankenbach et al*., 1989], deformable boundaries [e.g., *Schmeling et al*., 2008], or open box conditions approximating a semi-infinite fluid [e.g., *Olson et al*., 1993] have been used as well. We nevertheless lack a detailed comparison of the different assumptions on boundary conditions to better understand their role on plume dynamics.

[6] In this paper, we will combine laboratory models with numerical simulations to quantify the influence of the proximity and nature of boundary

conditions on the dynamics of a laminar thermal plume that rises from a small constant heater in a nearly constant-viscosity fluid. The experimental results obtained in finite domains will be compared to the theoretical predictions obtained in infinite fluid. This will enable us to discuss the limitations of the different techniques of investigation for mantle plume modeling.

1.2. Goal of the Paper

[7] This paper is one in a sequence of three. It follows up on *Vatteville et al*. [2009] and is a companion to *Vatteville et al*. (J. Vatteville et al., Development of a laminar thermal plume in a cavity, paper II, in preparation, *Journal of Fluid Mechanics*). This set of papers studies the formation of thermal plumes rising from a small heater in very viscous fluids. We use a combination of laboratory experiments (using silicone oils) and numerical simulations (using finite element methods). In *Vatteville et al*. [2009] we directly compared numerical simulations with the laboratory experiments for a single small box geometry. In paper II we consider the various stages of the plume formation, from the conductive growth of the boundary layer to the formation of the steady state plume.

[8] In the present paper, we consider the establishment of the steady state structure and how the boundaries of the box affect the plume structure. We will first review the theory of the velocity and thermal structure of thermal plumes at high Prandtl number Pr ($Pr = \nu/\kappa$, where ν is the kinematic viscosity and κ is the thermal conductivity). We will confirm the good comparison between laboratory models and numerical simulations [*Vatteville et al*., 2009]. We then use the numerical models to scale the models to much larger domains that would resemble laboratory experiments in very large tanks, with a viscous fluid filling a cavity that has no-slip (zero velocity) boundary conditions at the base and the sides, and a free-slip (zero normal velocity, zero tangential stress) boundary at the top. We will demonstrate that these boundary conditions play a crucial role in the formation of the plume structure. While the side boundaries become unimportant at a sufficiently large aspect ratio of the domain, the top free-slip boundary condition is important even at very large box sizes. We will finally show that a modification of the boundary conditions will allow for a good reproduction of the predicted structure for a semi-infinite fluid from independent theory [*Whittaker and Lister*, 2006a].

1.3. Predictions for the Stem Structure of a Laminar Plume at High Prandtl Number in a Semi-infinite Fluid

[9] *Batchelor* [1954] predicted that, for a steady state laminar plume rising from a point source in an infinite and constant viscosity fluid at infinite Prandtl number, the velocity at the plume axis V should be height-independent and scale with a typical velocity V_0:

$$V \sim V_0 = \left(\frac{g\alpha Q}{\rho C_p \nu}\right)^{\frac{1}{2}} \quad (1)$$

where g is the gravitational constant, α is the thermal expansion coefficient, Q is the power of the plume, ρ is the density, C_p is the specific heat and ν is the kinematic viscosity. The power of the plume is related to the temperature contrast ΔT between plume and ambient fluid and the plume velocity V. It can be found at any depth in the fluid from the horizontal integral

$$Q = 2\pi\rho C_p \int_0^\infty V \Delta T r dr \quad (2)$$

where r is the distance from the plume axis.

[10] A typical radius of the plume can be defined by a radius a outside of which the temperature anomaly is zero and inside which the temperature anomaly is quasi-constant. At high Pr the radius grows principally by diffusion and $a \sim \kappa t$ where t is time. Using the definition of a typical length scale L_0

$$L_0 = \left(\frac{\kappa^2 \rho C_p \nu}{g\alpha Q}\right)^{\frac{1}{4}} = \kappa / V_0 \quad (3)$$

we can write $a \sim (zL_0)^{\frac{1}{2}}$. *Fujii* [1962] suggested that at the center line of a plume at infinite Pr the temperature contrast varies as

$$\Delta T(r = 0) = \frac{Q}{4\pi k z} \quad (4)$$

where k is the thermal conductivity of the fluid and z is the height above the source.

[11] Using an asymptotic approach, *Worster* [1986] developed an analytical solution for the velocity and temperature contrast in the plume for fluids that have high, but not infinite Pr, which introduced an explicit Pr dependence in (1):

$$V = f(Pr) V_0 \quad (5)$$

where $f(Pr) = (\ln\varepsilon/2\pi)^{\frac{1}{2}}$ in which ε is the solution to the equation $\varepsilon^4 \ln(1/\varepsilon^2) = 1/Pr$ in the interval $0 < \varepsilon < e^{-\frac{1}{4}}$. In this analysis, the temperature contrast at the plume axis is given by (4).

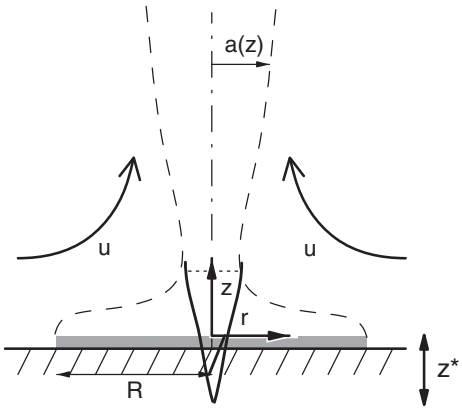

Figure 1. Modified from *Whittaker and Lister* [2006b]. Sketch of the steady state geometry of a plume rising from a disk heater of radius R. Above a certain height the temperature distribution in the plume is similar to that of a plume rising of a point heater at virtual depth z^*.

[12] In all cases above, the fluid is assumed to be infinite and the velocity is independent of the height above the source. *Whittaker and Lister* [2006a] developed a boundary layer theory for a very viscous plume rising from a point source that sits on a plane boundary. This semi-infinite geometry is more relevant to studies of plumes in natural or laboratory settings. *Whittaker and Lister* [2006a] derived that there is a typical height z_0 above the heater at which advection and diffusion are comparable:

$$z_0 = (32\pi)^{\frac{1}{2}} L_0 \approx 10 L_0 \quad (6)$$

and that above this height the plume radius and vertical velocity in the plume slowly increase with height:

$$a_{WL} \sim (z_0 z)^{\frac{1}{2}} [\ln(z/z_0)]^{-\frac{1}{4}} \quad (7)$$

and

$$V \sim V_0 [\ln(z/z_0)]^{\frac{1}{2}} \quad (8)$$

[13] The temperature in the plume center remains the same as (4).

[14] *Whittaker and Lister* [2006b] provided an extension of this study to that of a finite point source (Figure 1). In this case the temperature at the center of the plume is similar to that of (4) if it is assumed that there is a virtual point source at some depth $z^* < 0$ below the actual heater (see also *Shlien and Boxman* [1979] and *Shlien and Boxman* [1981]):

$$\Delta T(r=0) = C \frac{Q}{k(z-z^*)} \quad (9)$$

and

$$V = V_{WL} = C_v V_0 [\ln((z-z^*)/z_0)]^{\frac{1}{2}} \quad (10)$$

where we have introduced a proportionality constant C_v. The prediction for C remains equal to $C_w = \frac{1}{4\pi}$. We will refer to this set of predictions (9 + 10) of centerline velocity and temperature as WL06.

[15] The fluid dynamical experiments described in *Vatteville et al*. [2009] and used here are for finite Pr (5000–50,000) fluids in a confined tank. *Whittaker and Lister* [2006a] describe that inertial effects introduce secondary corrections to their theory, which become important at a radius of $z_0 Pr(\ln Pr)^{\frac{1}{2}}$. For our laboratory experiments and related numerical simulations this radius is well in excess of 10 m, which is obviously much larger than the laboratory dimensions. In the mantle, plumes carrying 20–300 GW [*Olson et al*., 1993] would feel inertial effects for radii greater than 10^{25} km. The infinite Pr description of [*Whittaker and Lister*, 2006a] should therefore be appropriate for plumes in the laboratory as well as in the mantle. Nevertheless, the confined medium introduces important influences of the side and top boundaries. Due to the high Pr nature of the fluid these are felt by the plume in its rise and development of steady state structure. This leads to a centerline velocity profile that is quite distinct from (10). It is our main goal in this paper to evaluate this difference quantitatively and to determine if we can approximate (10) better if (a) we simulate the plume evolution in boxes with very large aspect ratio (to minimize the effect of the side boundaries) and (b) use an open boundary condition at the top of the model (to minimize the effect of the top boundary).

2. Experiment Set Up

2.1. Laboratory Experiments

[16] The laboratory set up is the same as that discussed in *Vatteville et al*. [2009]. The heat source consists of a Peltier element covered by a 3 mm thick and 18 mm diameter copper disk. It is placed at the center of a tank with a rectangular base of dimension W^2 where W = 150 mm. The tank is filled with silicone oils (Rhodorsil 47V500 or 47V5000) to a height H = 165 mm (Figure 2a). The upper surface of the fluid is free and deformable. At time t = 0, a constant electric power P, ranging from 0.5 to 3.3 W, is applied to the heater. In steady state, this corresponds to heater temperature between 21 and 54°C.

[17] The silicone oils have nearly constant properties over the temperature range considered in the

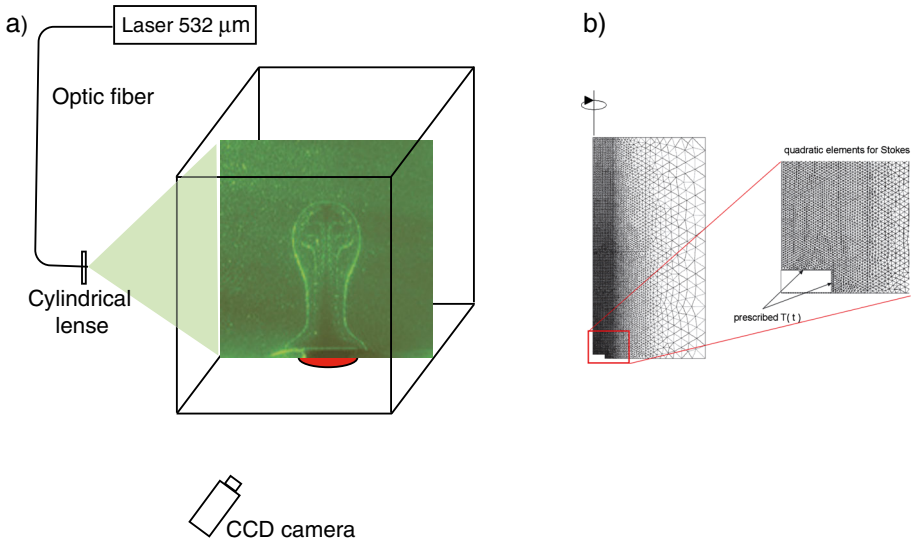

Figure 2. Experimental set-up: (a) laboratory experiments and (b) mesh used for the axisymmetric numerical simulations. The numerical resolution is finest around the heater with an average nodal point spacing of 0.2 mm.

experiments. The viscosity variation is less than a factor of three over the largest temperature range considered [*Vatteville et al.*, 2009].

[18] The fluid is seeded with 10 μm diameter glass spheres and two types of thermochromic liquid crystals. The thermochromic liquid crystals reflect light at different temperatures [*Davaille et al.*, 2011]. A vertical cross-section of the tank is illuminated by a 532 nm laser sheet and images are recorded every second using a CCD camera. Bright lines on the images of the laboratory experiments correspond to the two isotherms $24.1 \pm 1°C$ and $34.8 \pm 1.5°C$ (see *Davaille et al.* [2011] for details on the method and calibration).

[19] The velocity field was calculated by following the glass spheres using the particle-image-velocimetry package DaVis from LaVision. The resulting spatial resolution and amplitude precision were 2.5 mm and 0.1 mm/s (or 5% of the typical maximum velocity), respectively. Although the tank base is square, we verified that the thermal and velocity fields were axisymmetric by rotating the vertical laser cross-section [*Davaille et al.*, 2011].

2.2. Numerical Simulations

2.2.1. Model Geometry and Boundary Conditions

[20] The geometry for the numerical model is that of a cylindrical tank of height H and radius L. At the center of the base of the cylinder we model a small cylindrical heater with radius $R_{heater} = 9$ mm and height $h_{heater} = 3$ mm. We define the coordinate z as in Figure 1 with $z = 0$ corresponding to the top of the heater. We will use the coordinate y to indicate the distance from the base of the tank so that $y = z + h_{heater}$.

[21] We use two different sets of assumptions for geometry, boundary conditions, and fluid properties.

[22] In the first case we compare the models directly with the laboratory results and we mimic the lab conditions as closely as possible following *Vatteville et al.* [2009]. We use rigid bottom and side boundaries and a free-slip top surface. The volume of the tank is the same as that in the laboratory experiments with $H = 165$ mm and $L = 85$ mm. We use the measured fluid properties (see *Vatteville et al.* [2009, Table 1] for the fluids Rhodorsil 47V500 or 47V5000) and include the temperature-dependence of viscosity. The initial fluid temperature is the same as that in the corresponding laboratory experiments, and we prescribe the measured evolution of the temperature in the heater as boundary condition in the heat equation. The bottom and side boundaries are kept at constant (room) temperature. We verified for several powers that the steady state velocity and thermal structure did not depend on the initial heating history, since we obtained the same results by applying either a constant heat power or a constant temperature difference to the heater [*Vatteville*, 2009].

[23] In the second case, where we investigate the steady state plume structure for large domains, we use a large range of values for the height and radius of the tank. We model the fluid in the tank with the

same constant properties of the silicone oil Rhodorsil 47V500 but assume all properties (including viscosity) to be independent of temperature. The fluid initially is at uniform temperature T_{room} = 20°C. At time $t=0$ we set the heater instantaneously to a fixed temperature $T_{heater}=80$°C. We model the heater, the base of the model and the side boundaries as no-slip boundaries. The top of the model is either modeled as a free-slip boundary (vertical velocity and tangential stress are both zero) or as an "open" inflow-outflow boundary (normal stress and tangential stress are both zero). The smallest box corresponds to the size of the laboratory tank used in *Vatteville et al*. [2009] with height $H=0.165$ m and width $L=0.085$ m. We increase the height up to $H=1.28$ m and the width to $L=4.8$ m. Since we compute the temperature and velocity fields, we can determine the power Q by numerical integration of (2). For this 60°C temperature difference, the computed power varies from 2.44 to 2.47 W (1.4%), which shows that the size of the box has only a very minor influence on the power of the plume.

2.2.2. Governing Equations and Numerical Solution

[24] We solve the equations of conservation of mass, momentum, and energy for an incompressible fluid at infinite *Pr*:

$$\nabla \cdot \mathbf{u} = 0 \tag{11}$$

$$-\nabla P + \nabla \cdot \sigma = \rho\alpha(T - T_{room})\mathbf{g} \tag{12}$$

$$\rho C_p\left(\frac{\partial T}{\partial t} + \mathbf{u}\cdot\nabla T\right) = k\nabla^2 T \tag{13}$$

where $\sigma = \eta(\nabla \mathbf{u} + \nabla \mathbf{u}^T)$ is the stress tensor, η is dynamic viscosity, $\mathbf{u}$ is velocity, T is temperature, and $\mathbf{g}$ is gravity ($|\mathbf{g}|=9.8$ m/s^2). The nominal values for the fluid properties are $\rho=973$ kg/m^3, C_p = 1460 J/kg/K, $\alpha = 9.4\times10^{-4}$ 1/K, $k = 0.156$ W/mK, and $\eta = 0.4865$ Pa · s.

2.2.3. Numerical Solution

[25] The numerical solution of the governing equations is described in *Vatteville et al*. [2009]. Here we summarize the main points. The equations are solved using the finite element package Sepran [*Cuvelier et al*., 1986] in a two-dimensional axisymmetric geometry. We use a penalty function method for the Stokes and mass conservation equations and streamline upwinding for the heat equation. The finite element mesh is strongly refined near the heater (with a smallest grid spacing of 0.2 mm; Figure 2b). The grid spacing remains high to a distance of 10 cm from the heater beyond which it gradually decreases. At the symmetry axis the grid spacing increases to 0.5 cm (for the smallest heights used) or 2 cm (for the largest heights used) at the top of the box. Near the edges of the cylinder, where temperature is uniform and velocities are very small, the grid spacing increases to 25 cm for the largest boxes considered. This flexible gridding allows for the accurate yet efficient solution of the governing equations.

2.2.4. Dimensionless Parameters

[26] Our system can be characterized by a set of dimensionless parameters, which will be useful to compare the laboratory, numerical, and mantle cases. Besides *Pr*, we have the Rayleigh number that compares the driving thermal buoyancy forces to the resisting effects of thermal diffusion and viscous dissipation:

$$Ra = \frac{\alpha g \Delta T R^3}{\kappa \nu} \tag{14}$$

where R is the radius of the heater, which is a length scale close to the plume radius [e.g., *Griffiths*, 1986]. Here, *Ra* ranges between 2×10^2 and 7×10^3. Another definition of *Ra*, Ra_{RB} is obtained by using the total height of the box for the length scale and is commonly used in classical Rayleigh-Bénard convection in which the whole lower surface is at constant temperature. A value $Ra_{RB} \geq 10^6$ indicates that the box is much larger than the thermal boundary layers and that plume-shaped instabilities can develop. Here Ra_{RB} is between 10^6 (for the lab experiments with the V5000 oil) and 2×10^{10} (for the numerical simulations in the highest box). Using typical mantle values one can argue that Ra_{RB} probably ranges between 10^6 and 10^8.2. The aspect ratio of the box L/H ranges in the numerical simulation from 0.066 to 29.4, and from 0.45 to 0.55 in the laboratory experiments.3. The aspect ratio of the height of the box to the radius of the heater (H/R ranging from 18 to 133) and the ratio of the length of the box to the radius of the heater (L/R ranging from 8 to 533).

2.3. Plume Evolution to Steady State

[27] The development of the thermal plume is shown in Figure 3 for a typical numerical simulation with instantaneous heating with $\Delta T=60$°C, and in Figure 4 for a typical laboratory experiment with applied constant power to the heater. The

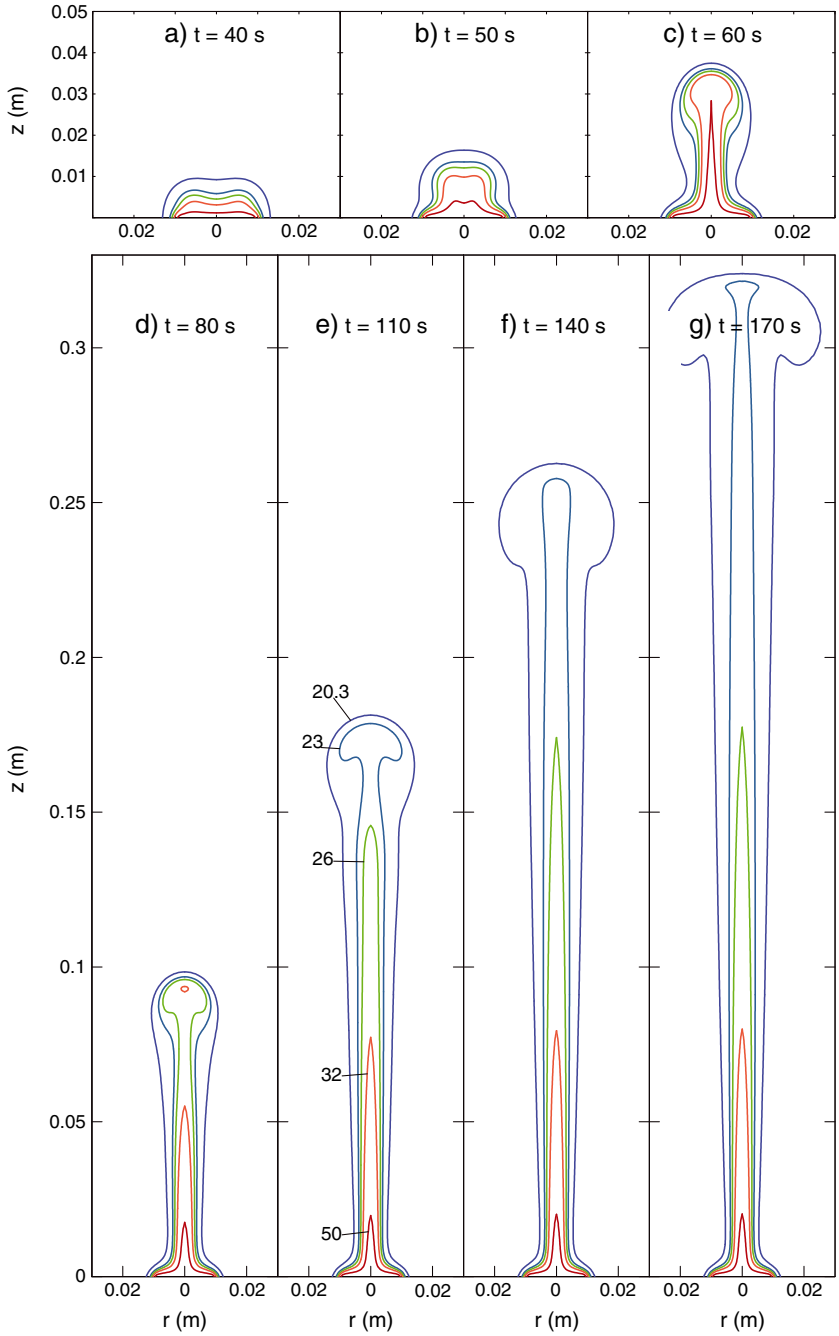

Figure 3. Plume evolution in a typical numerical simulation in an isoviscous fluid with similar properties to that of the silicone oil 47V500. Box has height $H = 33$ cm and width $L = 60$ cm. At time $t = 0$ s the heater boundary condition is changed from $T_{room} = 20°C$ to $T = 80°C$. The computed steady state power of the heater is 2.5 W. The contour values (in °C) are indicated in frame e); they represent temperatures at fractions 0.005, 0.05, 0.1, 0.2, and 0.5 of the temperature contrast between heater and room. In the initial stage the fluid becomes unstable more quickly at the edges of the heater, leading to the minor temperature inversion above the top of the heater.

structure and evolution present similar features in both cases.

[28] Since the heater has a finite size and extends a few millimeters above the bottom of the box, a strong lateral temperature gradient develops first at the edge of the heater, and therefore that is where the fluid becomes first unstable, leading to depression in the temperature contour lines above the heater axis in the early stages of the hot thermal boundary layer growth (Figures 3a and 3b). As the plume rises through the box the plume head grows

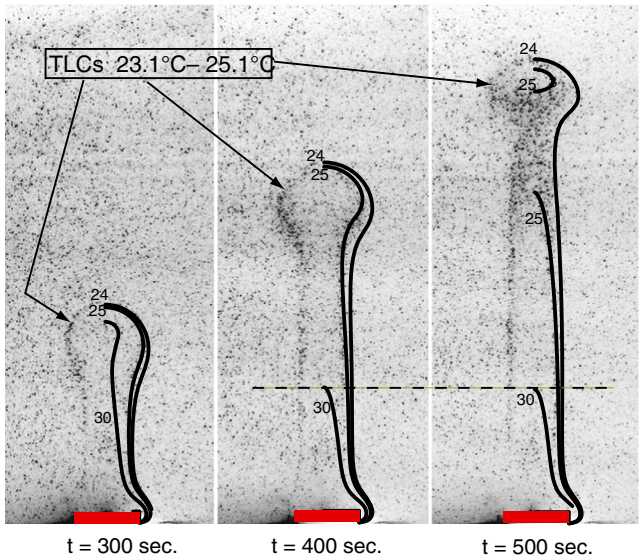

Figure 4. Snapshots of the temperature field at time $t = 300$ (a), 400 (b) and 500 (c) s in oil 47V5000 at power $P = 1.4$ W. The numerical simulation is run with the same properties of the fluid, same geometry, and same boundary conditions. In each frame the fuzzy background image provides the photo of the fluid where the thermochromic liquid crystals within the temperature range from 23.1 to 25.1°C show up in darker shades. The solid lines indicate the contours from the corresponding numerical model at 24, 25, and 30°C. Similar to Figure 3 the temperature structure of the plume stem reaches a steady state (as indicated by the dashed line).

and cools, while the plume stem that follows establishes a steady state structure relatively soon after the plume head has passed (Figures 3e–3g, Figures 4b–4c). The velocity profiles along the plume axis register a maximum, which is first located in the plume head (Figure 5), before jumping at the bottom of the plume stem when the plume head has sufficiently cooled down.

2.4. Comparison Between Laboratory and Numerical Models and Resolution Tests

[29] A systematic comparison of the laboratory experiments and their corresponding numerical simulations shows a good agreement between the two independent techniques [*Vatteville et al.*, 2009]. Numerical and laboratory isotherms coincide (Figure 4) and the evolution of the velocity field is found to be similar (Figure 5). Due to the thickness of isotherms obtained in silicone oils, the agreement on the thermal structure seen here is mainly qualitative. However, the velocity fields are much more accurately known and the profiles agree to within 5%. For the temporal evolution of the velocity maximum $V_m(t)$ along the plume axis, the agreement reaches 3% over the whole experiment (Figure 5b). The height of this velocity maximum is also well recovered by the two methods: although the laboratory data are noisier, the envelope of the points with velocity within 95% of $V_m(t)$ follows the numerical data (Figure 5a). The good agreement between the numerical simulations (performed without taking into account the inertial terms) and the laboratory experiments (at finite Pr) confirms that, for the parameter range of our study, inertial effects have no influence on plume dynamics. This result is consistent with observations already obtained in the case of Rayleigh-Bénard convection, whereby the convection characteristics seem independent of Pr as soon as $Pr > 100$ [*Krishnamurthi*, 1970a, 1970b; *Schmalzl et al.*, 2002; *Breuer et al.*, 2004].

[30] We perform a convergence test for the largest box. Figure 6 shows the velocity and temperature profiles along the plume axis for four different meshes. The overlap between the results obtained using the nominal resolution and those on the higher resolution meshes demonstrates that the models are well resolved in velocity and temperature.

3. Characterization of a (Near) Steady State Thermal Plume With Free Slip Top Boundary

[31] As the plume grows the convective flow in the box becomes increasingly box-filling. This is

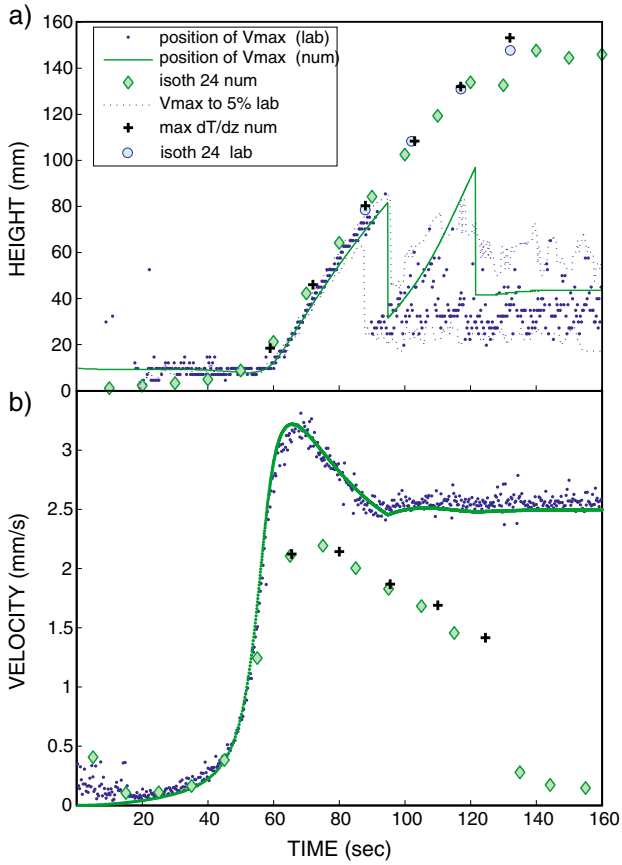

Figure 5. Comparison between numerical and experimental data in oil V500 ($P = 1.7$ W). Top: Evolution through time of (i) the position of maximum velocity on axis (dots for lab results, smaller dots to estimate 95% of that maximum, green line for numerical results) (ii) position of top of head outlined by isotherm 24°C (blue circles for lab results, green diamonds for numerical results), (iii) position of maximum temperature gradient (black crosses are numerical results) . Bottom: Evolution through time of (a) maximum velocity on axis (dots for lab results, green line for numerical results) (b) velocity of uplift of top of head (green diamonds are numerical isotherm 24°C, black crosses are maximum temperature gradient).

illustrated for the laboratory experiment by using time-lapse photography (Figure 7). The motion of the glass spheres causes streaks demonstrating how the fluid in the box is convecting. The side boundaries become important in this case between about 150 and 250 s while the plume is still in its initial stage of development. The top boundary becomes important between 340 and 550 s, which is long before the plume reaches the top boundary. The qualitative suggestion for the importance of the boundaries can be quantified by comparing how closely the models can reproduce the WL06 predictions for a semi-infinite space.

[32] The evolution of the temperature profile along the plume axis is shown in Figure 8 for plumes in numerical models with a free-slip top boundary. The two models shown here use the smallest and largest model domain used in this study. The temperature evolution is compared to the prediction (9; shown by the symbols) for the steady state plume temperature. Aside from the minor deviations in the plume head the theoretical prediction fits the plume stem temperature well during the development of the plume and the evolution toward the steady state.

[33] This raises an important question: if the presence of a top boundary is relatively unimportant in the comparison of temperature between numerical models and theory, does the same hold for the velocity profile? Or does the box filling effect shown in Figure 7 indicate a possible problem?

[34] In the remainder of this paper we will consider only the models with constant viscosity and a

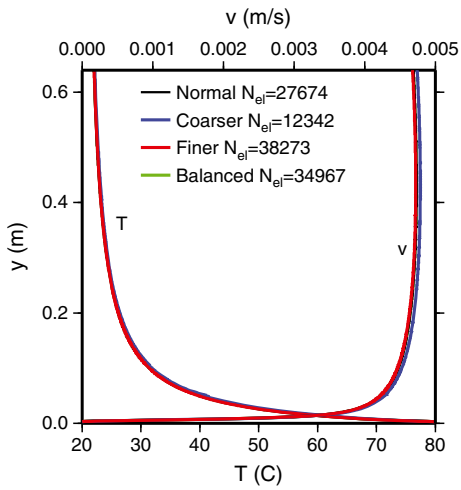

Figure 6. Convergence test for the model in the largest box ($H = 128$ cm; $L = 480$ cm). We show temperature and velocity for 4 different finite element meshes (N_{el} is the number of elements. The results for the mesh employed here is in black. Results in red show that for a finer grid (with approx. 1.5 times higher resolution). Results in blue are for a coarser grid. Results for a more balanced grid (with the same resolution as normal near the plume, but significantly higher resolution away from the plume compared to the normal grid) are shown in green. The overlap of the normal, finer and balanced grids show that the models in this paper are well resolved. Only at significantly lower resolution we see a divergence of the results.

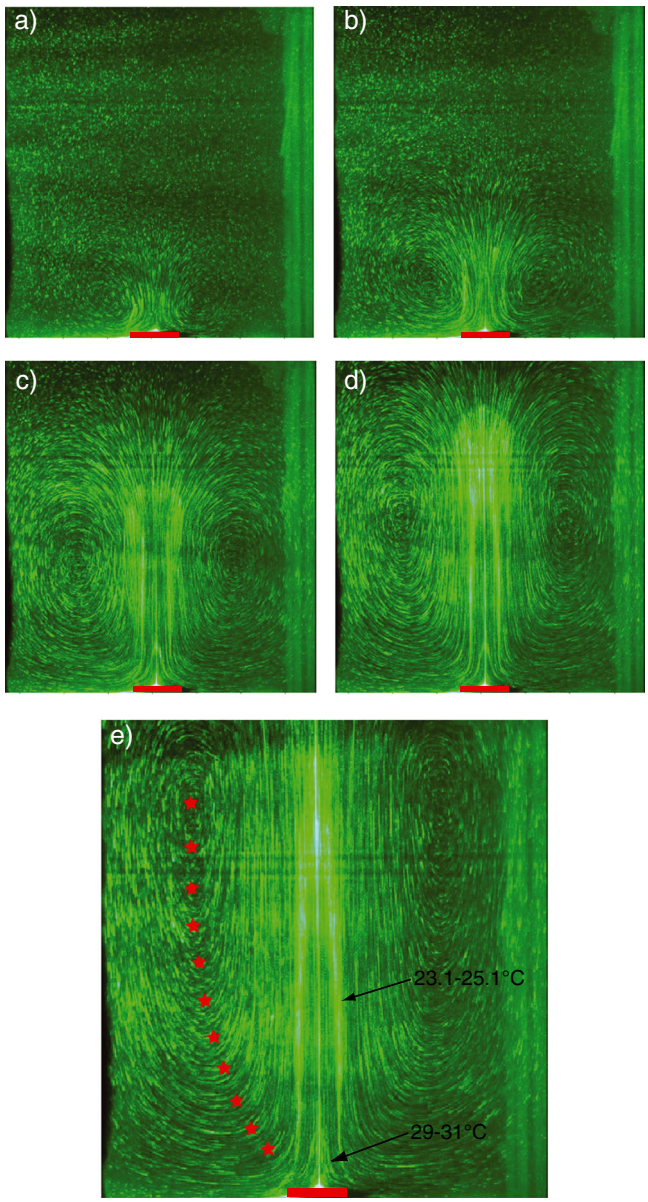

Figure 7. Time-lapse photographs showing the evolution of a laminar plume in oil V5000 with an electric power 1.17 W. The heater is outlined in red and provides the length scale (18 mm). (a) $t = 150$ s; (b) $t = 250$ s; (c) $t = 340$ s; (d) $t = 550$ s; (e) $t = 720$ s. As time increases the instability grows from an isolated state to a box filling plume. Red stars show the position of the rotation center over time. The black arrows show the two temperature ranges were the thermochromic liquid crystals become bright. The time-lapse pictures allow to follow the particle trajectories.

heater that is instantaneously heated to a constant temperature contrast of 60°.

3.1. Temperature Structure in Quasi Steady State

[35] We first will consider the temperature profile along the plume vertical axis at $t = 1000$ s as sufficiently close to that of the steady state structure. The plume has reached the top of the box for all heights considered (H = 16.5, 33, 65, and 128 cm). For each of these heights we consider a radius of the box of L = 8.5, 15, 30, 60, 120, 240, and 480 cm.

[36] We determine the power Q by numerical integration of (2). The power Q varies again very slightly, between 2.435 and 2.473 W (1.4%).

[37] We determine the constants A and z^* for each steady state temperature profile at the plume axis by

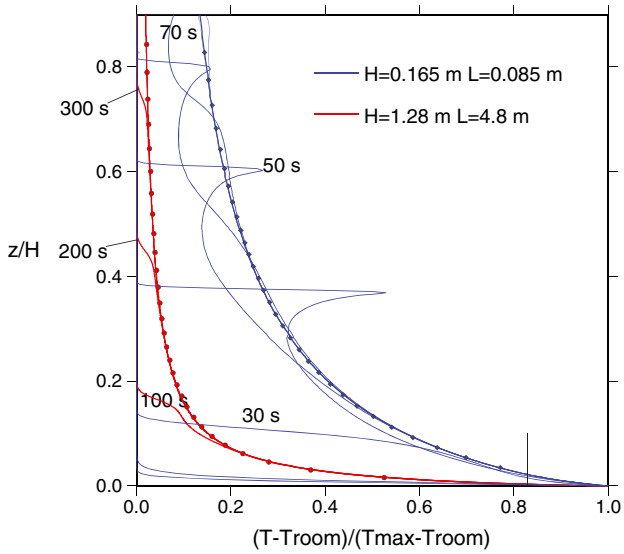

Figure 8. Evolution of a typical plume shown by the non-dimensional temperature contrast plotted at non-dimensional height. The evolution is shown for moderate power in both the smallest box (in blue) and largest box (in red) that we considered in this study. For the smallest box ($H = 16.5$ cm; $L = 8.5$ cm) we plot the plume temperature every 10 s; for the largest box ($H = 4.8$ m; $L = 1.28$ m) we plot the plume temperature every 100 s. The bold line represents the plume axis temperature at $t = 1000$ s which we take here to be sufficiently close to steady state. The theoretical fit to (9) for both examples is shown by the symbols. For the fit we use the temperature profile at 1000 s down from $z = 0.9H$ (top of frame) and up to a temperature of 50°C (thin vertical line). For the largest box we find $z^* = -0.02380$ and $C = 0.08779$. The root-mean-square (rms) misfit is 0.13°C with a maximum point-wise misfit of 4%. For the smallest box we find $z^* = -0.02420$ and $C = 0.08872$. The rms and maximum point-wise misfits are 0.10°C and 0.012% resp.

a nonlinear fit to (9). In this fit we exclude the lowermost (where $T > 70$°C and topmost (where $z > 0.9H$) parts of the temperature profile.

[38] Over the range of assumed steady state profiles, we find that the computed values z^* and C vary by only a few percent due to geometrical variations (see Appendix A). z^*/R_{heater} is around 2.65 and C is around 0.088. We note that our values for C are systematically higher (by about 9%) than the theoretical prediction $C_w = \frac{1}{4\pi} \approx 0.07958$.

[39] We show in Appendix A that the models also satisfy the WL06 prediction for the width of the thermal plume.

3.2. Velocity Profiles Along the Plume Axis

[40] We also compare the axial velocity profile with free-slip top boundary V to that of the prediction V_{WL} (10), where we determine V_0, and z_0 from the numerically integrated power Q and z^* from the temperature fit. We plot V (in red) and V_{WL} (in black) in the left-hand column of Figure 9 for variable H and L. The calculated velocity profile does not recover the small velocity increase predicted by the theoretical model. Instead, the velocity tends to stay quasi-constant, or to decrease with increasing height as the box becomes thinner.

[41] C_{v} is found where the theoretical prediction (10) and the model solution just touch (Figure 9). C_{v} ranges between 0.284 and 0.317 (see Appendix A). This leads to slightly variable predictions for the maximum of V_{WL} reached in each experiment (V_{max}) that tend for each tank height to reach a plateau value as $L/H \geq 2$ (Figure 10a). This value increases with increasing fluid thickness (Figures 9, 10a, and 10b).

[42] The right-hand column of Figure 9 shows the ratio V/V_{WL}. The modeled axial velocity fits the theoretical prediction only for a relatively short depth interval ($z \leq z_m \sim H/4$) and there is a strong deviation in the top half of the domain. However, since z_m increases with fluid thickness, this leads to an increase of V_{WL} predicted by equation (10), and therefore explain the increase in V_{max}/V_0 plateau values observed in Figures 10a and 10b, as H increases.

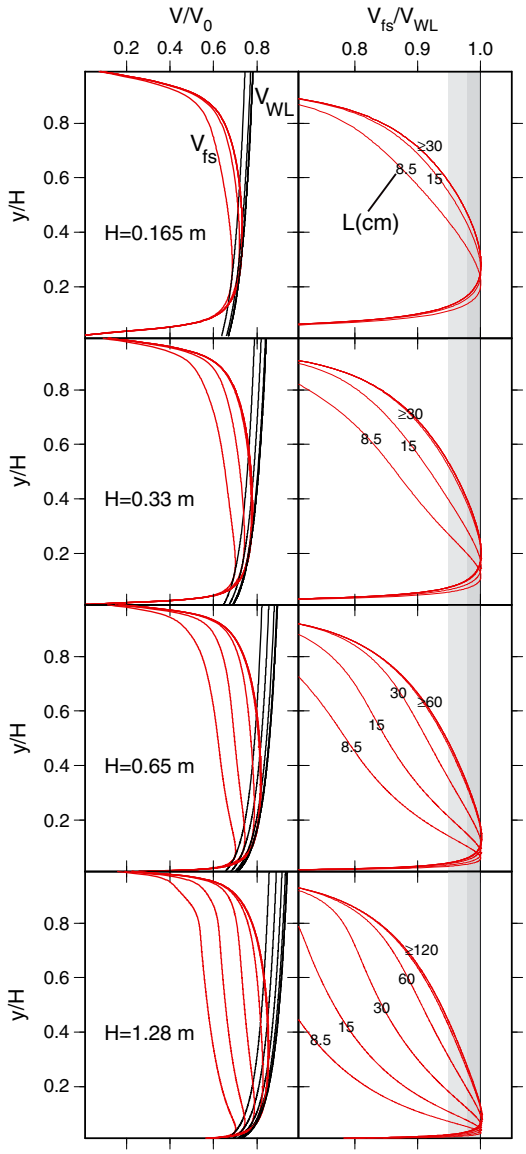

Figure 9. Comparison of modeled axial velocity V and prediction V_{WL} for variable H and L. In the left column we plot V/V_0 in red and V_{WL}/V_0 in black. The ratio V/V_{WL} is shown in red in the right column. The light grey band indicates where this ratio is >0.95. The dark grey band shows where this ratio is >0.98. The small numbers on the curves show the width of the box L (in cm).

3.3. Global Structure of the Flow

[43] From the numerical or laboratory velocity fields we calculated the stream function Ψ from our velocity fields using [*Tanny and Shlien*, 1985]:

$$\Psi(r,z) = \int_0^r rV_z(r,z)dr \qquad (15)$$

[44] As expected from the laboratory images (Figure 7), the stream function exhibits a maximum (Figure 11), the position of which coincides with the center of rotation of Figure 7.

[45] Investigation of the streamfunction extrema confirms that the side boundaries become unimportant for aspect ratios $L/H \geq 2$ (see Appendix A).

[46] Close examination of the evolution of the stream function through time shows the development of weak cold instabilities from the top of the box where the temperature is kept at 20°C (Figure 12). Given the axisymmetric nature of the plume, it means that the hot plume impact, and the subsequent spreading of its hot head below the top surface, triggers the descent of a ring of cold material around its rim. This has previously been reported for classical Rayleigh-Bénard convection [*Olson et al.*, 1988; *Androvandi et al.*, 2011].

[47] This phenomenon causes a long term drift of the temperature. The stream function for earlier times is symmetric but then settles to an asymmetric pattern with slightly lower convective vigor and lower z_{max}. It appears that for the small box of Figure 12, the steady pattern is reached when $t \geq$ 4000 s. This long term drift in the solution makes it clear that all of the results shown above are only in a quasi steady state. The models could be integrated for significantly longer times but that would impose to take into account the influence of the thermal boundary condition at the top surface. Although this is potentially relevant for applications of plumes rising in the silicate mantles of the terrestrial planets, it makes a direct comparison with existing models and theories difficult. It is more optimal to render this thermal top boundary effect less important. In the following section we will describe how we achieve this with a change from the (lab- and mantle-relevant) free slip and isothermal boundary condition to that of an outflow boundary, where material can freely move in and out of the top boundary, as to simulate plume evolution in a semi-infinite fluid.

4. Evolution to a Steady State Thermal Plume With Open Top Boundary

[48] To simulate an open top boundary, we prescribe a top boundary condition for the Stokes equations with zero normal stress and zero tangential stress. For the heat equation we assume a natural boundary condition for a segment out to half the width of the box where we expect the flow to be out the box. For larger radii we assume a constant temperature boundary condition so that the return flow will bring constant temperature fluid into the model domain. In this case the heat brought up by the plume is advected out of the computational

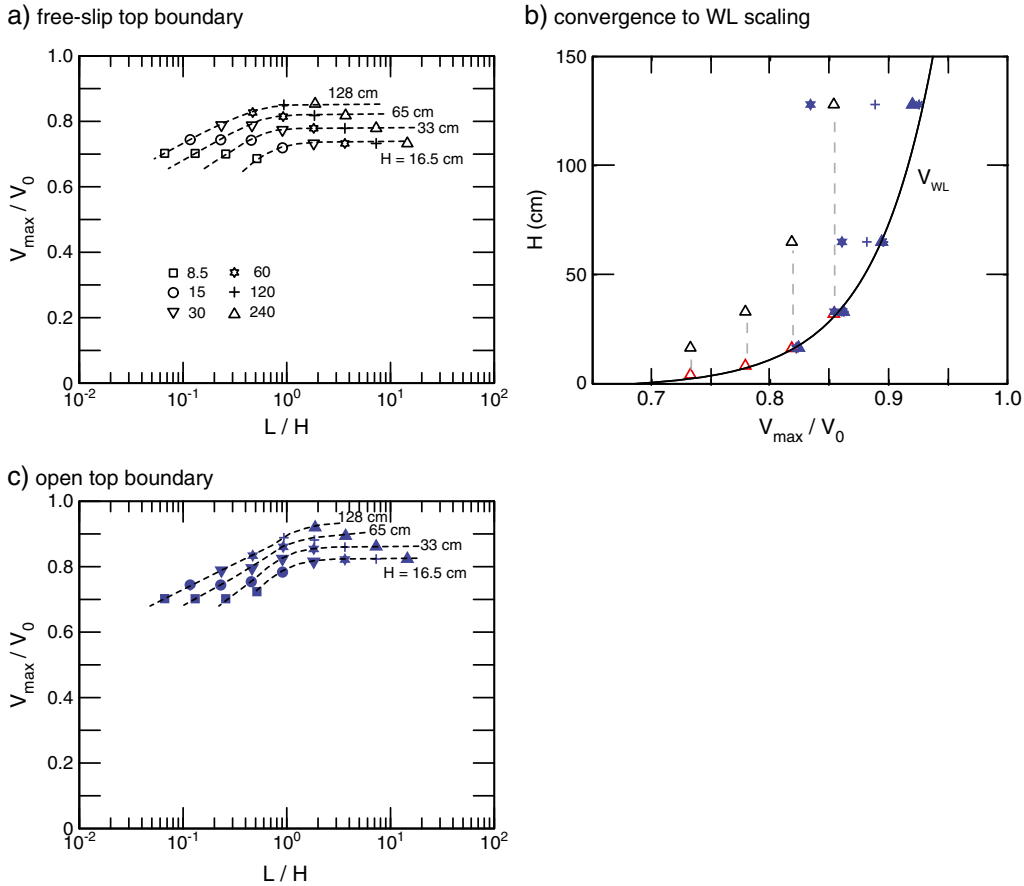

Figure 10. Maximum velocity along the plume axis compared for the two cases with free-slip and open top boundary. (a) Maximum velocity V_{max} for the free slip configuration normalized by Batchelor velocity scale, as the function of the domain height (indicated by H. Symbol type indicates the domain width L, identified (in cm) in the legend. (b) V_{max}/V_0 for the largest domain width ($L=60$ through $L=240$ cm) for different fluid heights. In blue the open boundary case and in black the free surface case. The red symbols indicate the real depths at which the velocity was maximum (see Figure 9) in the free surface case with $H=240$ cm. The solid black line represents Whittaker and Lister's scaling (10) with $C_v=0.313$. (c) Maximum velocity V_{max} for the open top boundary configuration normalized by Batchelor velocity scale, as the function of the domain aspect ratio.

domain. The spreading of hot fluid under the top boundary that is seen with the free-slip boundary is absent and we do not see a long term drift due to the adjustment of this boundary. Instead, we find robust steady state flow patterns as soon as the plume head has been advected out of the domain.

4.1. Thermal Structure

[49] In this case we find that the computed power varies from 2.43 to 2.55 W, which represents a slightly larger range than with the free-slip top boundary (2.44–2.47 W). The values for $-z^*/R_{heater}$ and C are very close to those obtained for the free-slip boundary and range from 2.63 to 2.72 (3.3%) and 0.08702 to 0.0893 (2.5%), respectively.

[50] At this stage we do not understand the reason for the small but systematic difference between the theoretical prediction for C and those obtained in our experiments. Using further numerical models we have explored whether the heater geometry is responsible for the slight misfit, but we did not find any significant differences with a heater that had a smaller radius, or with a heater that was aligned flush with the bottom boundary. In fact, once the plume has emerged from the thermal boundary layer (i.e., $z \gg z_0$) the thermal and velocity structure follow the same trends as described above, irrespective of the details of the heat sources, such as radius or thickness.

4.2. Velocity Structure

[51] The streamfunction and centerline velocities obtained with the open top boundary are shown in Figures 13 and 14. The side boundary remains

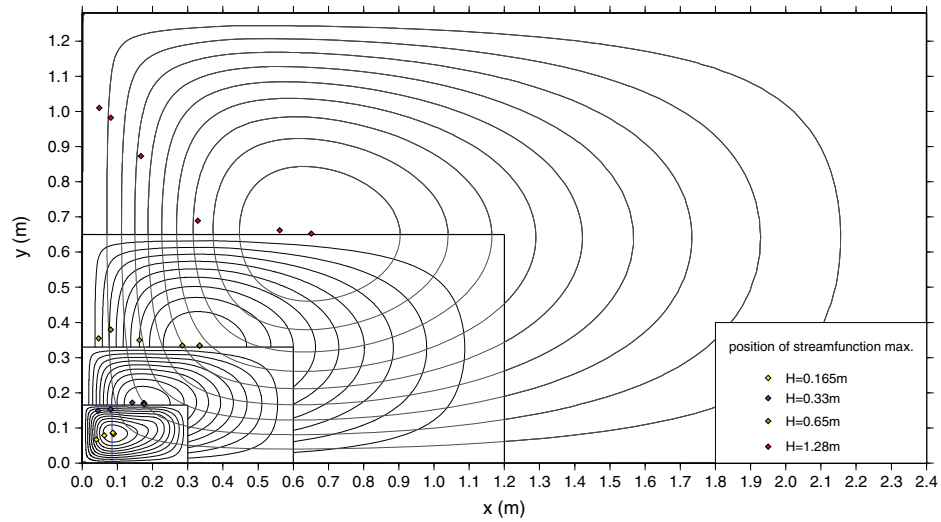

Figure 11. Streamfunction for variable H at $t = 1000$ s. The position of the streamfunction maximum is plotted by the diamonds. The position of this extremum tends towards $x = y = H/2$ for $L/H \geq 2$. For clarity we plot the streamfunction for each height in the box with $L/H \sim 2$. the streamfunction contours are for 10 equidistant intervals to the streamfunction maximum, with $\psi_{max} = 8 \cdot 10^{-6}$, $3 \cdot 10^{-5}$, $1.1 \cdot 10^{-4}$, and $3.4 \cdot 10^{-4}$ for $H = 16.5$, 33, 65, and 128 cm, respectively. The blue box in the lower left corner indicates the size of the smallest box used in this study. The largest box used in the study is twice as wide as the largest frame.

important for small aspect ratio ($H/L \leq 2$). We note however an excellent agreement (to within 2%) with the theoretical prediction (WL06) for $H/L \geq 2$ (Figures 14, 10b, and 10c). There remains only a small influence of the top boundary in the conduit near the very top of the domain. This suggests that the change to an open boundary is sufficient to render unimportant the strong effects on velocity

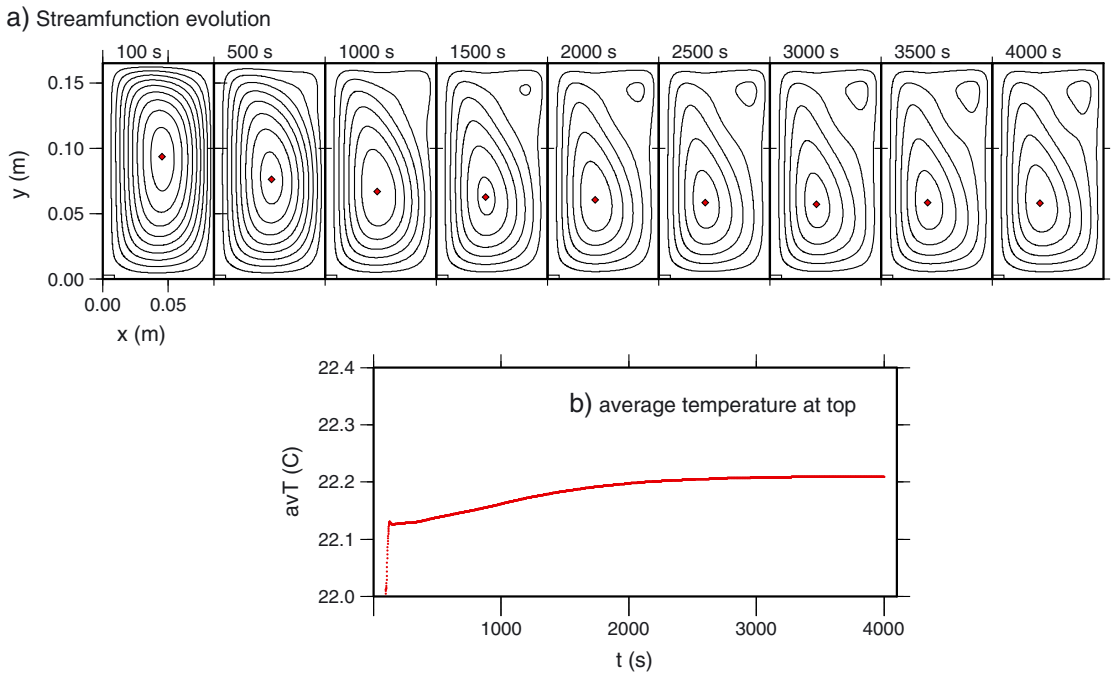

Figure 12. (a) Evolution until $t = 4000$ s of the streamfunction (a) in the smallest box ($H = 16.5$ cm, $L = 8.5$ cm). After an initial apparent steady state with symmetrical streamfunction the pattern becomes asymmetric. (b) average temperature in a rectangle in the top left corner of 5 mm wide by 2 mm high.

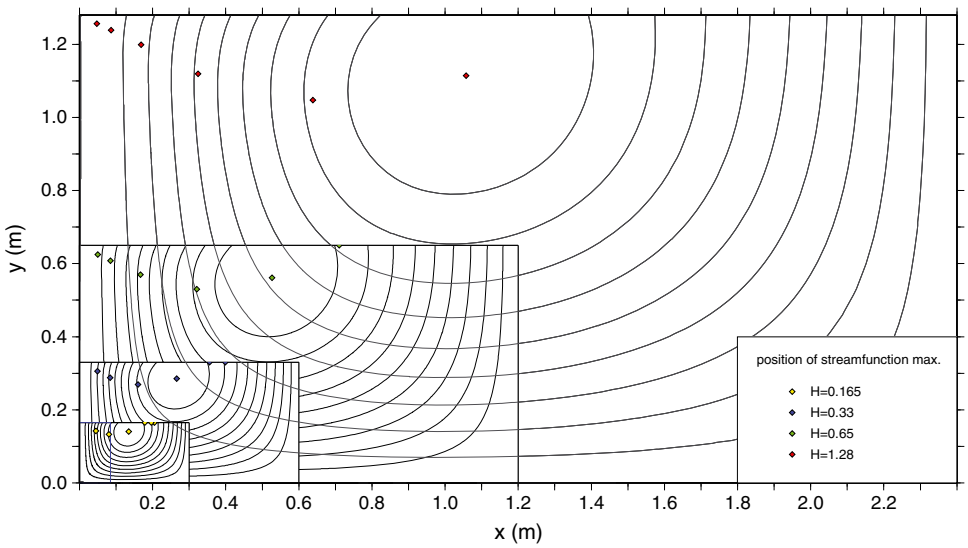

Figure 13. As Figure 11 but now with an open top boundary. The streamfunction contours are for 10 equidistant intervals to the streamfunction maximum, with $\psi_{max} = 2.3 \cdot 10^{-5}$, $8.5 \cdot 10^{-5}$, $3.2 \cdot 10^{-4}$, and $1.2 \cdot 10^{-3}$ for $H = 16.5$, 33, 65, and 128 cm, respectively.

seen in the models with the free-slip top boundary. In this case, the velocity scale becomes independent of H and is well described by:

$$V(z) = 0.313 V_{WL} f(L,z) \quad (16)$$

where $f(L,z)$ describes the influence of the side rigid boundaries. The proximity of the side boundaries are increasing the drag on the plume and decreasing its upwelling velocity. For a cylinder or a sphere of radius a moving along the axis of a cylinder of radius L, the drag increase (and therefore the velocity decrease of the cylinder/sphere) is a function of the ratio a/L [*Happel and Brenner*, 1973]). Now, we verified that in the open boundary case, the radius of the thermal plume is also well predicted by $a_T(z) = 0.480 a_{WL}(z)$, and so increases with z. Hence, a_T/L increases with depth, and the velocity should decrease accordingly. Figure 15 shows the velocity reduction measured in our experiments for the largest fluid depth (e.g., Figure 14) compared to the predictions for the sphere [*Happel and Brenner*, 1973, pp. 318] and the cylinder [*Happel and Brenner*, 1973, pp. 342]. We see that the magnitude of velocity reduction observed for the thermal plume is intermediate between the two theoretical cases.

5. Discussion

[52] We can now attempt to apply this study to mantle plumes and mantle convection. In doing so, we have to keep in mind several potential shortcomings. First, there is no laterally confined heater at the core-mantle boundary, which instead is an interface where the temperature is uniformly hot. However, the presence of denser, compositionally heterogeneous, material on the core-mantle boundary can act to modulate this uniform thermal boundary condition, forming hot "piles" on the core-mantle boundary. Moreover, these piles could be enriched in radiogenic elements, which would increase their heating potential (for a review see *Garnero and McNamara* [2008]). Long-lived plumes have been shown to develop preferentially on and around those piles [*Tackley*, 1998; *Namiki and Kurita*, 1999; *Davaille*, 1999; *Davaille et al.*, 2002; *Jellinek and Manga*, 2002; *Tan et al.*, 2002; *McNamara and Zhong*, 2005]. Our small heater can be regarded as a simplified mantle "pile."

[53] Another concern is the nearly constant viscosity we consider in our study, while mantle material has a strongly temperature-dependent viscosity and mantle plumes are therefore often assumed to be much less viscous than the ambient mantle. The near-constant viscosity plumes considered here may nevertheless be appropriate since it has been suggested that hot plumes viscosity may not be significantly lower due to the effect of grain size variations in the lower mantle. In extreme cases, variations of the grain size could be so large that hot plume could be more viscous than ambient mantle because of enhanced grain growth with increasing temperature [e.g., *Solomatov et al.*, 2002; *Korenaga*,

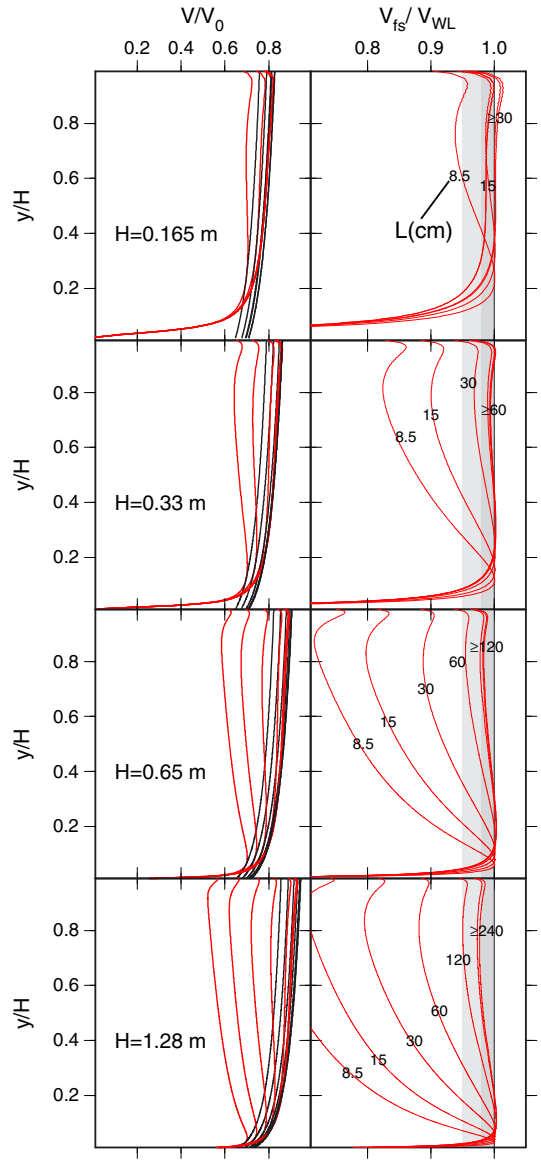

Figure 14. As Figure 9 but now for open top boundary. The plume center line velocity for large aspect ratio shows a significantly better match with the theoretical prediction (WL06).

2005]. Besides, although seismic tomography is still struggling to image plumes, recent results of finite frequency tomography are showing slow anomalies of 200 to 400 km width under certain hotspots [e.g., *Montelli et al.*, 2004], which would be more compatible with plumes as viscous or more viscous than the ambient mantle. Therefore, our simplified constant viscosity study can be of interest for mantle plumes.

[54] Given the mantle conditions, we expect plumes with Rayleigh numbers Ra_{RB} around $10^6 - 10^8$, which is the situation that we encountered in our shortest boxes (cf. section 2). In that case, our study suggests that care should be taken when applying the results for Stokes flow in a half-space to the confined geometries of the Earth's mantle, particularly when velocities are considered. The application of theoretical, laboratory, and numerical simulations should be significantly more robust for temperature in the plumes.

[55] The strong importance of the boundaries has important applications to the interpretation of geodynamical results. For example, it is common to study the subduction of oceanic lithosphere by modeling the sinking of dense or cold boundary layers into a viscous medium. Due to restrictions in laboratory experiments (where the boundaries are essential) or due to computational limitations the geometries employed often have rigid or free-slip boundaries that do not allow the fluid to enter or leave through the boundaries. A number of papers have highlighted that the sinking of a slab can induce a strong toroidal component around the slab [see, e.g., *Buttles and Olson*, 1998; *Piromallo et al.*, 2006; *Jadamec and Billen*, 2010]. A study that employed outflow boundary conditions (similar to those in this paper) concluded that the toroidal flow was significantly reduced [*Kneller and van Keken*, 2008]. Most likely this is due to the fact that with

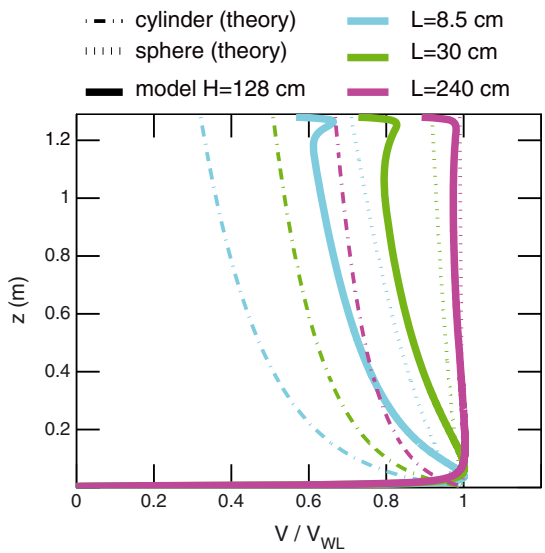

Figure 15. Comparison between V/V_{WL} observed in the open boundary simulations (solid lines) and the drag reduction predicted for a sphere (short dash lines [*Happel and Brenner*, 1973, pp. 318]) or for a cylinder (dot-dashed lines [*Happel and Brenner*, 1973, pp. 342]) for $H = 128$ cm.

open boundaries the fluid below a slab can escape, whereas in a finite box it can only move around the slab. The toroidal flow is then effectively generated by the non-outflow boundary. In the Earth, the dynamics is more complicated. While the free-slip or rigid boundary conditions confine and influence the flow, the open boundary conditions do not represent the fact that the Earth's mantle is confined to a spherical geometry and that slabs and plumes influence each other over long distances. The use of full spherical geometry is still computationally expensive, particularly if one wishes to accurately resolve mantle dynamics at the present-day convective vigor of the Earth [*Stadler et al*., 2010]. The use of a cylindrical geometry [*van Keken*, 2001; *Gérault et al*., 2012] or other two-dimensional approximations to the spherical Earth [*Hernlund and Tackley*, 2008], where the models take into account at least in part the curvature of the Earth and the connectedness of the Earth mantle, are therefore still attractive options.

6. Conclusions

[56] We have performed a series of well-resolved numerical simulations of a steady state plume rising from a localized heat source in a cavity. For models with a free-slip top boundary we see significant differences with theoretical predictions for the centerline velocity of plumes rising from the same heater in an infinite half-space. The effect of the side boundaries is negligible for aspect ratios of two or larger, but the effect of the free-slip top boundary conditions affects the plume solution for a significant part of its height. We can better approximate these half-space solutions by modifying the free slip boundary to a stress-free boundary, which simulates an open boundary condition. In this case we find that for significantly high aspect ratio the theoretical prediction for velocity is matched to within 2%.

[57] The differences between the theoretical predictions for temperature and those obtained from the numerical simulations are significantly less sensitive to the size of the domain and the choice of top boundary conditions. In fact, the parameters that determine the shape of the centerline temperature profile are nearly constant across the range of models.

Appendix A

[58] Here we summarize a few technical points and provide background information on some of the observations that we provided in the main paper.

[59] The parameters that govern the fit of the predicted centerline temperature to the theory are provided in (Figure A1). In general we find that

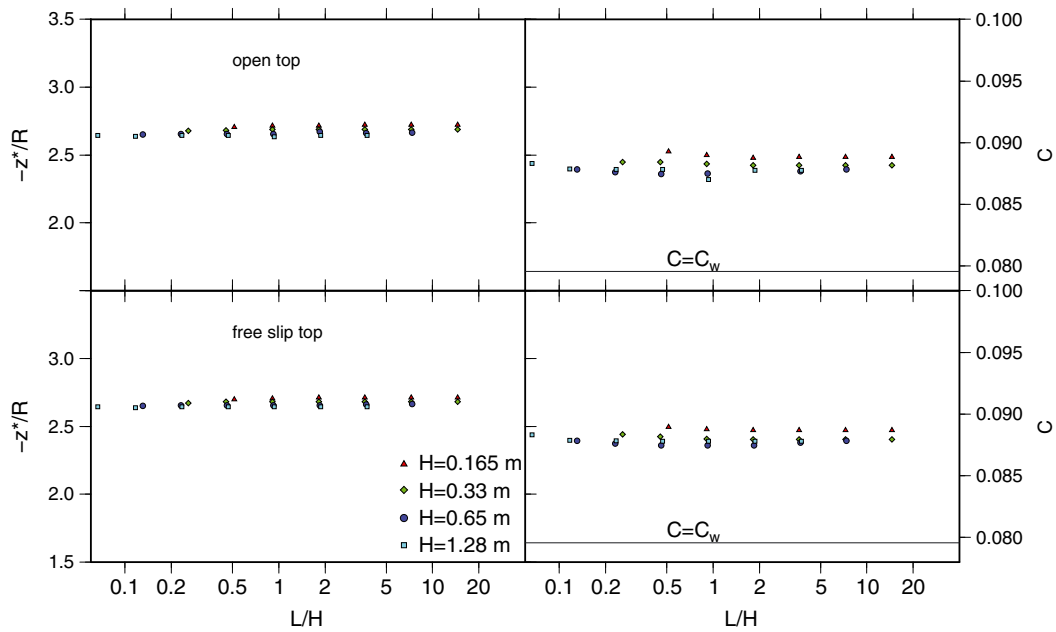

Figure A1. The parameters z* (left) and C (right) as determined from the centerline temperature profile by a nonlinear fit to equation 9. While the size of the box and the choice of top boundary conditions have a significant effect on the velocity, the temperature in the plume is principally insensitive to these geometrical considerations.

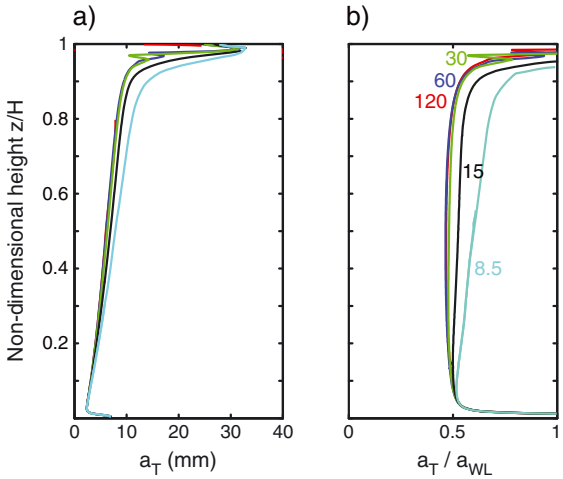

Figure A2. a) Radius of the thermal anomaly calculated with (1) as a function of depth for H = 65 cm for various choice of L. b) Radius of the thermal anomaly a_T divided the WL06 scale a_{WL}. For L > 30 cm and away from the top and bottom boundaries, the two radii are proportional with $a_T = 0.480a_{WL}$. The width of the model L is indicated (in cm) in frame b). Cyan curve is for $L = 8.5$ cm, black for L = 15 cm, green for L = 30 cm, blue for L = 60 cm, red for L = 120 cm.

these values are similar when $L/H \geq 2$ but change slightly as a function of H. This suggests that the top boundary has the dominant influence on the plume structure and that the side boundary becomes unimportant for aspect ratios larger than two. The range of $-z^*/R_{heater}$, and C are 2.639–2.711 (2.7%) and 0.08745–0.0889 (1.7%), respectively (Figure A3).

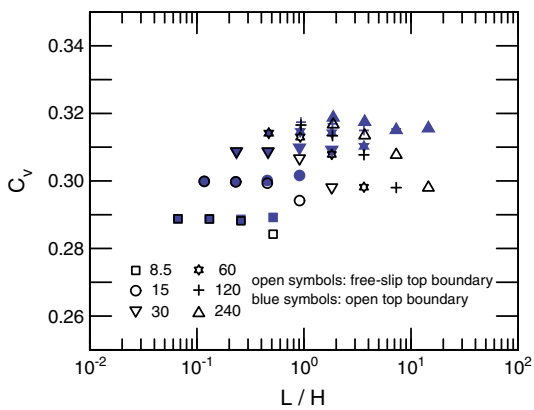

Figure A3. Constant C_v in the velocity scaling (10) determined for the free slip (black symbols) and the open boundary (blue symbols) cases. Domain width L is indicated (in cm) in the legend for the different symbols.

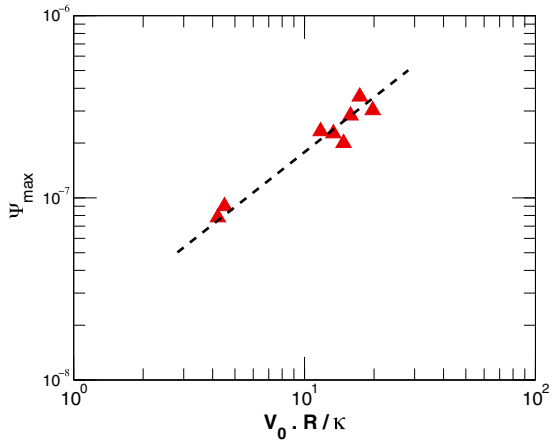

Figure A4. Maximum value of the stream function as a function of the Batchelor velocity scale V0 for the laboratory experiments with oils V5000 and oils V500.

[60] Following *Whittaker and Lister* [2006a], we define the width of the thermal plume as the variance of the temperature distribution:

$$a_T(z)^2 = \frac{\int_0^L \Delta T(r,z) r^3 dr}{\int_0^L \Delta T(r,z) r dr}. \quad \text{(A1)}$$

[61] Figure A2 shows that the plume thermal radius calculated with (A1) is well predicted by WL6 model (7) with $a_T = 0.480 a_{WL}$ for $H/L \geq 0.5$.

[62] The values for C_v that are determined by taking the theoretical prediction (10) where it just touches to the model solution is shown in Figure 9.

[63] For given domain dimensions (L, H), the value of the stream function maximum Ψ_{max} is proportional to V_0 (Figure A4). As the domain aspect ratio L/H increases, we find two very well defined trends (Figure A5).

[64] For $L/H \geq 2$, the stream function maximum scales as $\Psi_{max} = (0.05 \pm 0.005) V_0 H^2$ and its position becomes close to $x_{max} \simeq z_{max} \simeq H/2$ ($x_{max} = (0.53 \pm 0.04)H$ and $z_{max} = (0.51 \pm 0.04)H$). This is the case where the side boundaries are far enough from the plume for both the stream function maximum value and its position to be independent of the box radius L.

[65] On the other hand, when $L/H \leq 2$, the side boundaries becomes increasingly important for the plume dynamics and we have (for $L/H \leq 0.5$)

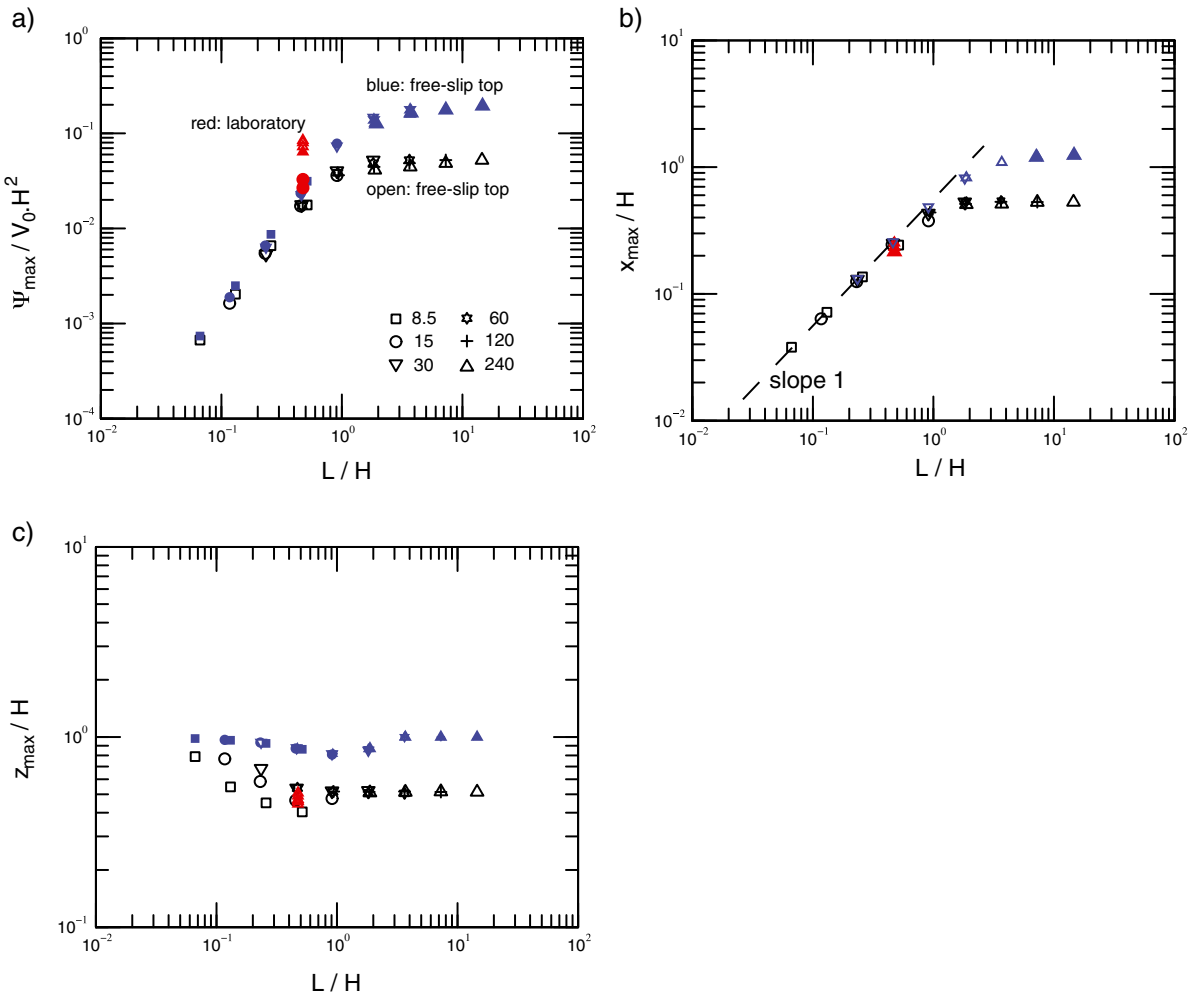

Figure A5. Characteristics of the stream function maximum as a function of the domain aspect ratio. In black, the numerical experiments with a free surface, in blue the ones with the top open boundary, in red the laboratory experiments for temperature differences between 21 and 54°C. Symbols indicate the width of the models (indicated in cm in the legend in frame a). a) non-dimensional streamfunction maximum, b) non-dimensional horizontal position of maximum, c) non-dimensional height.

$x_{max} = (0.54 \pm 0.05)L$. The values for z_{max} are much more scattered (Figure A5), especially for small boxes.

Acknowledgments

[66] This work was supported by the French ANRs "BeGDY" (ANR-06-BLAN-0109) and "PTECTO" (ANR-09-BLAN-0142), the program DyETI from INSU/CNRS, and by the US National Science Foundation under grant number EAR-0855487. The manuscript was improved thanks to the comments of Norm Sleep, Shijie Zhong and Paul Tackley.

References

Androvandi, S., A. Davaille, A. Limare, A. Fouquier, and C. Marais (2011), At least three scales of convection in a mantle with strongly temperature-dependent viscosity, *Phys. Earth Planet. Int.*, *188*, 132–141.

Batchelor, G. K. (1954), *An Introduction to Fluid Dynamics*, Cambridge University Press, Cambridge, UK.

Bercovici, D., and J. Mahoney (1994), Double flood basalts and plume head separation at the 660-kilometer discontinuity, *Science*, *266*, 1367–1369.

Blankenbach, B., et al. (1989), A benchmark comparison for mantle convection codes, *Geophys. J. Int.*, *98*, 23–38.

Breuer, M., S. Wessling, J. Schmalzl, and U. Hansen (2004), Effect of inertia in Rayleigh-Bénard convection, *Phys. Rev. E.*, *69*, 026302.

Buttles, J., and P. Olson (1998), A laboratory model of subduction anisotropy, *Earth Planet. Sci. Lett.*, *164*, 245–262.

Chay, A., and D. J. Shlien (1986), Scalar field measurements of a laminar starting plume cap using digital processing of interferograms. *Phys. Fluids*, *29*, 2358–2366.

Couliette, D. L., and D. E. Loper (1995), Experimental, numerical and analytical models of mantle starting plumes, *Phys. Earth Planet. Inter.*, *92*, 143–167.

Cuvelier, C., A. Segal and A. A. van Steenhoven (1986), *Finite Element Methods and the Navier-Stokes Equations*, Reidel, Dordrecht, The Netherlands.

Davaille A. (1999), Simultaneous generation of hotspots and superswells by convection in a heterogeneous planetary mantle, *Nature*, *402*, 756–760.

Davaille A., F. Girard, and M. Le Bars (2002), How to anchor plumes in a convecting mantle? *Earth Plan. Sci. Lett.*, *203*, 621–634.

Davaille, A., and A. Limare (2004), Laboratory studies of mantle convection, in: *Mantle Dynamics*, edited by D. Bercovici, pp. 89-165, vol. *7*, Treatise of Geophysics, edited by G. Schubert, Elsevier, The Netherlands.

Davaille, A., A. Limare, F. Touitou, I. Kumagai, and J. Vatteville (2011), Anatomy of a laminar starting thermal plume at high Prandtl number, *Exp. Fluids*, 285–300.

Farnetani, C. G., and H. Samuel (2005), Beyond the thermal plume paradigm, *Geophys. Res. Lett.*, *32*, 07311, doi:10.1029/2005GL022360.

Fujii, T. (1962), Theory of the steady laminar natural convection above a horizontal line heat source and a point heat source, *Int. J. Heat Mass Transf.*, *6*, 597–606.

Garnero, E., and A. K. McNamara (2008), Structure and dynamics of the Earth's lower mantle, *Science*, *320*, 626–628.

Gérault, M., T. W. Becker, B. J. P. Kaus, C. Faccenna, L. Moresi, and L. Husson (2012), The role of slabs and oceanic plate geometry in the net rotation of the lithosphere, trench motions, and slab return flow, *Geochem. Geophys. Geosyst.*, Q04001.

Griffiths, R. W. (1986), Thermals in extremely viscous fluids, including the effects of temperature dependent viscosity, *J. Fluid Mech.*, *166*, 115–138.

Griffiths, G. W., and I. H. Campbell (1990), Stirring and structure in mantle starting plumes, *Earth Planet. Sci. Lett.*, *99*, 66-78.

Happel, J., and H. Brenner (1973), *Low Reynolds Number Hydrodynamics*, Noordhoff, Leiden, The Netherlands.

Hernlund, J., and P. J. Tackley (2008), Modeling mantle convection in the spherical annulus, *Phys. Earth Planet. Inter.*, *171*, 48–54.

Hwang, Y. K., J. Ritsema, P. E. van Keken, S. Goes, and E. Styles (2011), Wavefront healing renders deep plumes seismically invisible, *Geophys. J. Inter.*, *187*, 273–277, doi:10.1111/j.1365-246X.2011.05173.x.

Ito, G., and P. E. van Keken (2007), Hotspots and melting anomalies, in: *Mantle Dynamics*, edited by D. Bercovici, pp. 371–345, Vol. 7, Treatise on Geophysics, edited by G. Schubert, Elsevier, The Netherlands.

Jadamec, M. A., and M. I. Billen (2010), Reconciling surface plate motions with rapid three-dimensional mantle flow around a slab edge, *Nature*, *456*, 338–339.

Jellinek, A. M., and M. Manga (2002), The influence of a chemical boundary layer on the fixity, spacing and lifetime of mantle plumes, *Nature*, *41*, 760–763.

Kaminski, E., and C. Jaupart (2003), Laminar starting plumes in high-Prandtl-number fluids, *J. Fluid Mech.*, *478*, 287–298.

King, S. D., and J. Ritsema (2000), African hotspot volcanism: small-scale convection in the upper mantle beneath cratons, *Science*, *290*, 1137–1140.

Kneller, E. A., and P. E. van Keken (2008), Effect of three-dimensional slab geometry on deformation in the mantle wedge: implications for shear wave anisotropy, *Geochem. Geophys. Geosyst*, *9*, Q01003.

Korenaga, J. (2005), Firm mantle plumes and the nature of the core-mantle boundary region. *Earth Planet, Sci. Lett.*, *232*, 29–37.

Krishnamurthi, R. (1970a), On transition to turbulent convection. 1. Transition from 2-dimensional to 3-dimensional flow, *J. Fluid Mech.*, *42*, 295–307.

Krishnamurthi, R. (1970b), On transition to turbulent convection. 2. Transition to time-dependent flow, *J. Fluid Mech.*, *42*, 309–320.

Kumagai, I. (2002), On the anatomy of mantle plumes: effect of the viscosity ratio on entrainment and stirring. *Earth Planet. Sci. Lett.*, *198*, 211–224.

Kumagai, I., A. Davaille, K. Kurita, and E. Stutzmann (2008), Mantle plumes: thin, fat, successful, or failing? Constraints to explain hot spot volcanism through time and space, *Geophys. Res. Lett.*, *35*, L16301, doi:10.1029/2008GL035079.

Laudenbach, N., and U. R. Christensen (2001), An optical method for measuring temperature in laboratory models of mantle plumes. *Geophys. J. Int.*, *145*, 528–534.

Lin, S.-C., and P. E. van Keken (2005), Multiple volcanic episodes of flood basalts caused by thermochemical plumes, *Nature*, *436*, 250–252, doi:10.1038/nature03697.

McNamara, A. K., and S. Zhong (2005), Thermochemical structures beneath Africa and the Pacific Ocean, *Nature*, *437*, 1136–1139.

Montelli, R., G. Nolet, F. Dahlen, G. Masters, E. R. Engdahl, and S.-H. Hung (2004), Finite-frequency tomography reveals a variety of plumes in the mantle, *Science*, *303*, 338–343.

Morgan, W. J. (1971), Convection plumes in the lower mantle, *Nature*, *230*, 42–43.

Moses, E., G. Zocchi, and A. Libchaber (1993), An experimental study of laminar plumes, *J. Fluid Mech.*, *251*, 581–601.

Namiki, A., and K. Kurita (1999), The influence of boundary heterogeneity in experimental models of mantle convection, *Geophys. Res. Lett.*, *26*, 1929–1932.

Olson, P., and H. Singer (1985), Creeping plumes, *J. Fluid Mech.*, *158*, 511–531.

Olson, P., G. Schubert, C. Anderson, and P. Goldman (1988), Plume formation and lithosphere erosion: a comparison of laboratory and numerical experiments, *J. Geophys. Res.*, *93*, 15,065–15,084.

Olson, P., G. Schubert, and C. Anderson (1993), Structure of axisymmetric plumes, *J. Geophys. Res.*, *98*, 6829–6844.

Piromallo, C., T. W. Becker, F. Funiciello, and C. Faccenna (2006), Three-dimensional instantaneous mantle flow induced by subduction, *Geophys. Res. Lett.*, *33*, L08304.

Ribe, N., A. Davaille, and U. Christensen (2006), Fluid mechanics of mantle plumes, in: *Mantle Plumes: A Multidiscipinary Approach*, edited by J. Ritter and U. Christensen, pp. 1–47, Springer, Heidelberg, Germany.

Rogers, M. C., and S. W. Morris (2009), Natural versus forced convection in laminar starting plumes, *Phys. Fluids*, *21*, 083601.

Schmalzl, J., M. Breuer and U. Hansen (2002), The influence of the Prandtl number on the style of vigorous thermal convection, *Geophys. Astrophys. Fluid Dyn.*, *96*, 381–403.

Schmeling, H., A. Y. Babeyko, A. Enns, C. Faccenna, F. Funiciello, T. Gerya, G. J. Golabek, S. Grigull, B. J. P. Kaus, G. Morra, S. M. Schmalholz, and J. van Hunen (2008), A benchmark comparison of spontaneous subduction models - towards a free surface, *Phys. Earth Planet. Inter.*, *171*, 198–223.

Shlien, D. J. (1976), Some laminar thermal and plume experiments, *Phys. Fluids*, *19*, 1089-1098.

Shlien, D. J. and R. L. Boxman (1979), Temperature-field measurement of an axisymmetric laminar plume, *Phys. Fluids*, *22*, 631–634.

Shlien, D. J. and R. L. Boxman (1981), Laminar starting plume temperature-field measurement, *Int. J. Heat Mass Transf.*, *24*, 919–931.

Solomatov, V. S., R. El-Khonzondar, and V. Tikare (2002), Grain size in the lower mantle: constraints from numerical modeling of grain growth in two-phase systems, *Phys. Earth Planet. Inter.*, *129*, 265-282.

Stadler, G., M. Gurnis, C. Burstedde, L. C. Wilcox, L. Alisic, and O. Ghattas (2010), Dynamics of plate tectonics and mantle flow: from local to global scales, *Science*, *329*, 1033–1038.

Tackley, P. J. (1998), Three-dimensional simulations of mantle convection with a thermo-chemical basal boundary layer: D, in *The Core-Mantle Boundary Region, Geodynamics Series*, vol. 28, edited by M. Gurnis, M. E. Wyssession, E. Knittle, and B. A. Buffett, pp. 231-253, American Geophysical Union, Washington, D.C.

Tan, E., M. Gurnis, and L. J. Han (2002), Slabs in the lower mantle and their modulation of plume formation, *Geochem. Geophys. Geosyst.*, *3*, 1067.

Tanny, J., and D. J. Shlien (1985), Velocity field measurements of a laminar starting plume, *Phys. Fluids*, *28*, 1027–1032.

Thompson, P. F., and P. J. Tackley (1998), Generation of mega- plumes from the core-mantle boundary in a compressible mantle with temperature-dependent viscosity. *Geophys. Res. Lett.*, *25*, 1999–2002.

Turner, J. S. (1962), The starting plume in neutral surroundings, *J. Fluid Mech.*, *13*, 356–368.

van Keken, P. E. (1997), Evolution of starting mantle plumes: a comparison between numerical and laboratory models, *Earth Planet. Sci. Lett.*, 1–14.

van Keken, P. E. (2001), Cylindrical scaling for dynamical cooling models of the Earth, *Phys. Earth Planet. Inter.*, *124*, 119–130.

Vasquez, P. A., A. T. Perez, and A. Castellanos (1996), Thermal and electrohydrodynamics plumes. A comparative study. *Phys. Fluids*, *8*, 2091–2096.

Vatteville, J., P. E. van Keken, A. Limare, and A. Davaille (2009), Starting laminar plumes: comparison of laboratory and numerical modeling, *Geochem. Geophys. Geosys.*, *10*, Q12013.

Vatteville, J. (2009), Dynamique des panaches thermiques laminaires: application aux panaches mantelliques, Ph.D. Thesis, Institut de Physique du Globe, Paris, France.

Whitehead, J. A., and D. S. Luther (1975), Dynamics of laboratory diapir and plume models, *J. Geophys. Res.*, *80*, 705–717.

Whittaker, R. J., and J. R. Lister (2006a), Steady axisymmetric creeping plumes above a planar boundary. Part 1. A point source, *J. Fluid Mech.*, *567*, 361–378.

Whittaker, R. J., and J. R. Lister (2006b), Steady axisymmetric creeping plumes above a planar boundary. Part 2. A distributed source, *J. Fluid Mech.*, *567*, 379–397.

Wolfe, C. J., S. C. Solomon, G. Laske, J. A. Collins, R. S. Detrick, J. A. Orcutt, D. Bercovici, and E. H. Hauri (2009), Mantle shear-wave velocity structure beneath the Hawaiian hot spot, *Science*, *326*, 1388–1390.

Worster, M. G. (1986), The axisymmetric laminar plume: asymptotic solution for large Prandtl number, *Stud. Appl. Math*, *75*, 139–152.